Optical Materials 73 (2017) 290–305

Contents lists available at ScienceDirect

Optical Materials

journal homepage: www.elsevier.com/locate/optmat

Synthesis, DFT band structure calculations, optical and photoelectrical characterizations of the novel 5-hydroxy-4-methoxy-7-oxo-7*H*-furo [3,2-g]chromene-6-carbonitrile (**HMOFCC**)

Magdy A. Ibrahim [a], Shimaa Abdel Halim [a], N. Roushdy [b], A.A.M. Farag [c, d, *], Nasser M. El-Gohary [a]

[a] Department of Chemistry, Faculty of Education, Ain Shams University, Roxy, 11757, Cairo, Egypt
[b] Electronics Materials Dep., Advanced Technology& New Materials Research Inst., City of Scientific Research & Technological Applications (SRTA-City), New Borg El-Arab City, P.O. Box: 21934, Alexandria, Egypt
[c] Physics Department, Faculty of Science and Arts, Aljouf University, Aljouf, Saudi Arabia
[d] Thin Film Laboratory, Physics Department, Faculty of Education, Ain Shams University, Roxy, 11757, Cairo, Egypt

ARTICLE INFO

Article history:
Received 8 March 2017
Received in revised form
10 August 2017
Accepted 14 August 2017

Keywords:
6-Formylvisnagin
Ring transformation
TD-DFT theoretical investigation
UV-spectra
Spectral data
Optoelectronic application

ABSTRACT

Reaction of 4-methoxy-5-oxo-5*H*-furo[3,2-g]chromene-6-carboxaldehyde (**1**) with hydroxylamine hydrochloride resulted in ring transformation producing the novel 5-hydroxy-4-methoxy-7-oxo-7*H*-furo [3,2-*g*]chromene-6-carbonitrile (**HMOFCC**). The structure was deduced based on its correct elemental analysis and spectral data (IR, ^{1}H NMR, ^{13}C NMR and mass spectra). The geometries of the **HMOFCC** were completely optimized by means of DFT-B3LYP/6-311++G (d,p) theoretical level. The ground state properties such as; total energy, the energy of HOMO and LUMO and Mulliken atomic charges were also determined. In addition, the two solvents; polar (methanol) and nonpolar (dioxane) were utilized to extract the electronic absorption spectra. The assignment of the detected bands was discussed by TD-DFT calculations. A cauliflower-like, as well as, needle-like leaves morphologies were observed using scanning electron microscope images. Two direct optical band gaps were extracted from the photon energy dependence of absorption coefficient at the band edges and found to be 1.16 and 2.56 eV. A characteristic emission peak of photoluminescence spectrum was observed and shifted depending on the solvent type. A remarkable rectification characteristic of **HMOFCC**/p-Si heterojunction confirms the diode-like behavior. The main important parameters like series resistance, shunt resistance and reverse saturation current show illumination dependence under influence of the illumination intensity range 20 −100 mW/cm^2. The heterojunction based **HMOFCC** showed phototransient properties under various illumination intensities which give the recommendation for the studied heterojunction in the field of optoelectronic device application.

1. Introduction

The natural occurring khellin (4, 9-dimethoxy-7-methyl-5*H*-furo [3, 2-*g*] chromen-5-one) [1], obtained from the fruits and seeds of *Ammi visnaga* L., possesses a high antiatherosclerotic and lipid-altering activity [2]. Khellin has been used for the photochemotherapeutic treatment of vitiligo and psoriasis [3]. The photodynamic characteristics of khellin in its photoreaction with DNA were previously investigated by Trabalzini et al. [4]. Generally, furochromones are known to have anti-inflammatory and analgesic [5–7], antitumor [8] and antimicrobial activities [9].

Eiden et al. [10] have investigated the structure of 6-formylvisnagin (4-methoxy-5-oxo-5*H*-furo[3,2-g]chromene-6-carboxaldehyde) as a one of the most important categories of Khellin. Another condensed studies have been achieved by Ibrahim et al. [11–14] for the chemical characteristics of γ-pyrone fused benzene as well as quinolin-2(1*H*)-ones [15,16]. As an extension of this type of studies, the present investigation aims to explore the chemical reactivity of 6-formylvisnagin towards a hydroxylamine hydrochloride and consider the optical absorption characteristics of

* Corresponding author: Physics Department, Faculty of Science and Arts, Aljouf University, Aljouf, Saudi Arabia.
E-mail address: alaafaragg@gmail.com (A.A.M. Farag).

http://dx.doi.org/10.1016/j.optmat.2017.08.017
0925-3467/

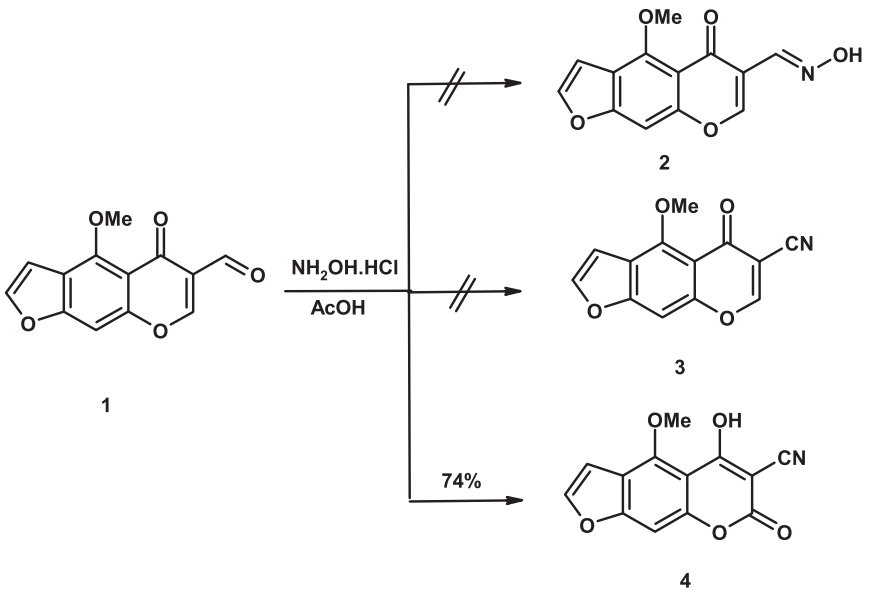

Fig. 1. Reaction of 6-formylvisnagin with hydroxylamine hydrochloride.

the synthesized product and its applications. El Harmoudi et al. [17] have reported the characterization of chitin and chitosan by infrared spectroscopy, nuclear magnetic resonance and theoretical calculation of UV–Vis spectra. They proposed theoretical approach depending on geometry optimization and relating quantum chemical calculations based on semi-empirical PM3 method within a framework of the confined Hartree–Fock approach. In addition, Arslan et al. [18] have calculated the vibrational frequencies and geometric parameters of the 5-chloro-10-oxa-3-thia-tricyclo [5.2.1.0^{1,5}]dec-8-ene-3,3-dioxide (COTDO) compound in the ground state to recognize the essentials from the exploratory vibrational frequencies and geometric parameters by utilizing the Hartree-Fock and density functional using Becke's three-parameter hybrid method with the Lee, Yang, and Parr correlation functional methods (B3LYP) with the standard 6-31G(d,p) and 6-311G(d,p) basis sets. Moreover, El Kouari et al. [19] have presented the theoretical calculations of UV spectra and second-order frequency-dependent molecular hyperpolarizability to propose NLO analysis of Anthocyanin's derivatives on a molecular scale. They explored that the quantum chemical calculations results can furnish the rule for finding of acquiescence of the calculated and experimental electronic properties in these types of molecules.

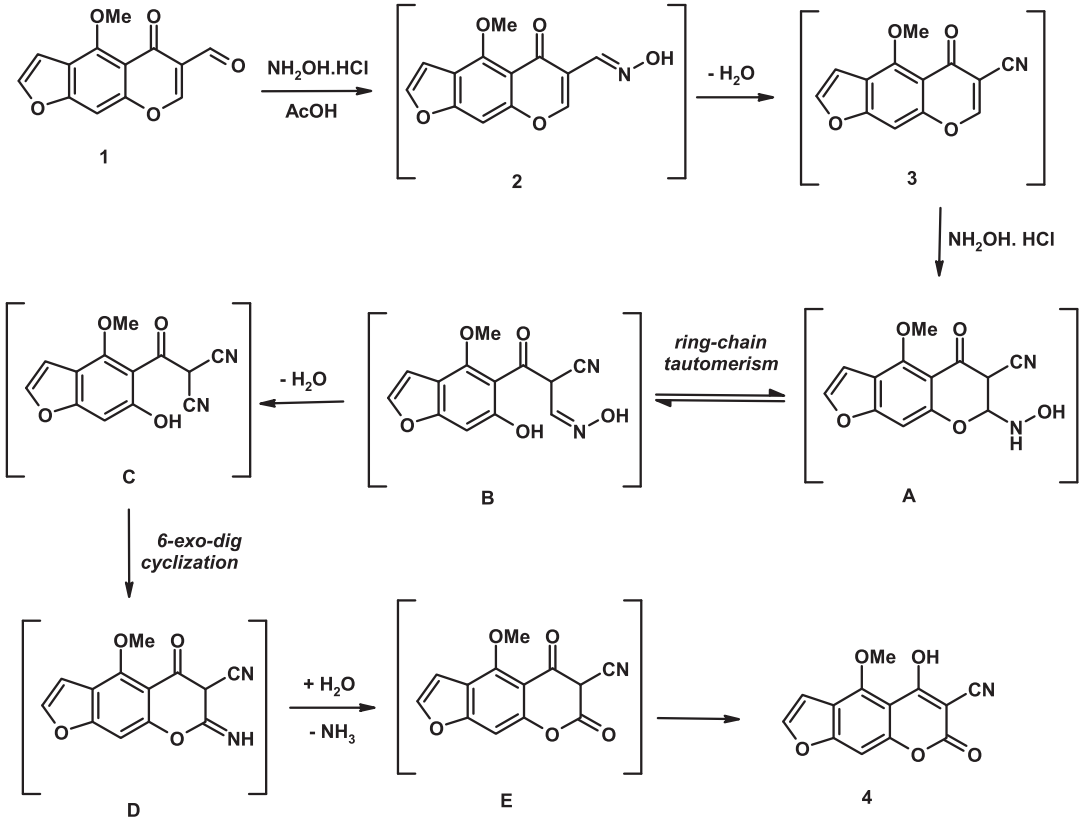

Fig. 2. The proposed mechanism for the formation of **HMOFCC**.

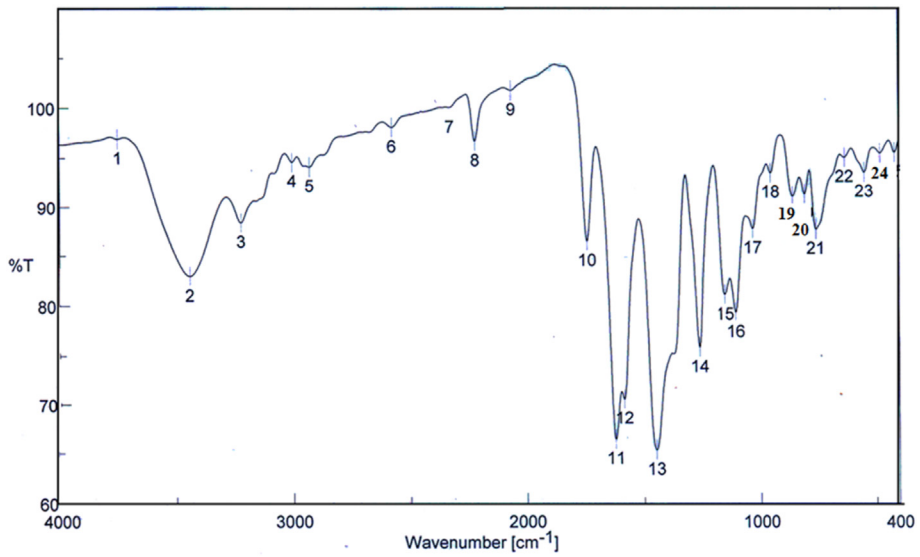

Fig. 3. The IR spectrum of **HMOFCC**.

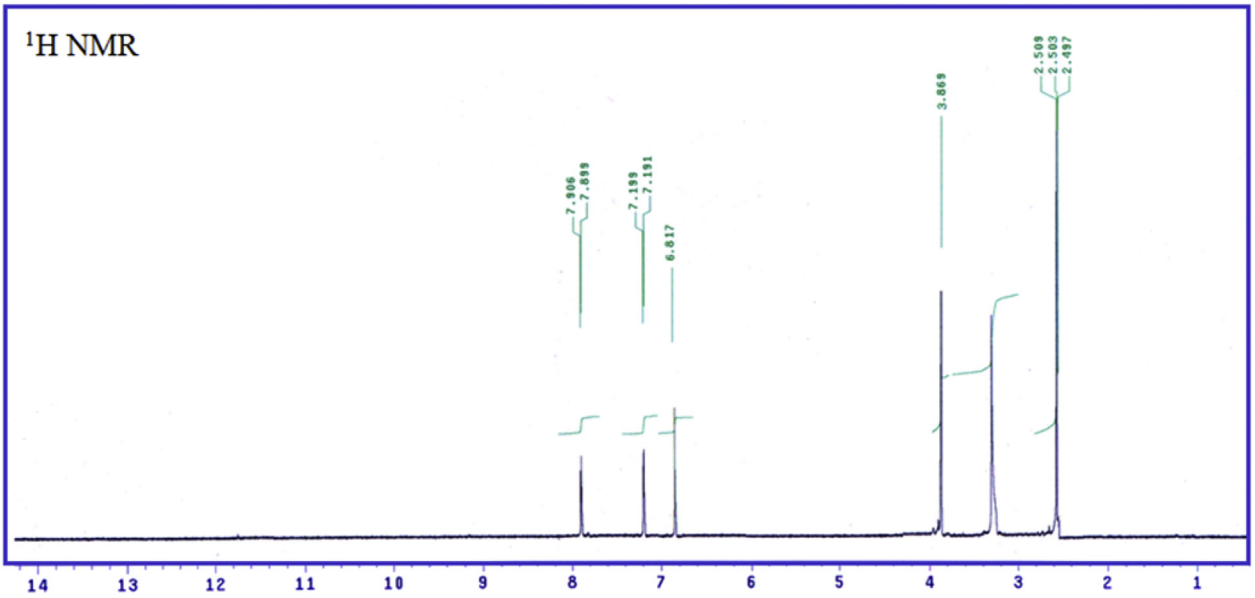

Fig. 4. The ^{1}H NMR spectrum of **HMOFCC**.

The theoretical calculation can give an insight into some of these issues since it can determine the structure of the molecules, the active sites, and atomic level description of interaction mechanisms on the intermediate formation involved in a given reaction [20–23]. Recently, because of their high accuracy theoretical calculations have also significantly contributed to drug discovery and design [24–26]. In the present work, synthesis of 5-hydroxy-4-methoxy-7-oxo-7H-furo[3,2-g]chromene-6-carbonitrile (**HMOFCC**) is considered and the confirmation for the structure is investigated. Also, the theoretical DFT calculations have been carried out the equilibrium geometry of the synthesized compounds. In addition for investigation; (i) optimized geometries of the starting compound **1** and the product; 5-hydroxy-4-methoxy-7-oxo-7*H*-furo[3, 2-g]chromene-6-carbonitrile (**HMOFCC**), as well as the other compounds **2** and **3**. (ii) Basis set on geometrical parameter and methods of calculation effects. (iii) Dipole moment and atomic charge. (iv) Energetic of the molecules. (v) TD-DFT calculations illustrated the effect of solvent polarity on the observed spectra and hence, predicting the relative stabilities, extent of charge transfer character and the assignment of the detected bands can be explained as localized, delocalized and/or of charge transfer (CT). The electronic absorption and emission spectra of molecules usually supported by the electronic structure of the compound. This manifestation enables the detailed understanding of the forces that govern the electronic structure of the studied compound (**HMOFCC**). The spectrophotometric measurements for elucidating the optical constants of the prepared films in a wide spectral range are investigated. Moreover, the characteristics of the **HMOFCC**-based photodiode characterization are also considered.

2. Experimental details

*2.1. Preparation and molecular structural characterizations of **HMOFCC***

To a hot solution of carboxaldehyde **1** (0.50 g, 2 mmol) in acetic acid (15 mL), hydroxylamine hydrochloride (0.14 g, 2 mmol) in

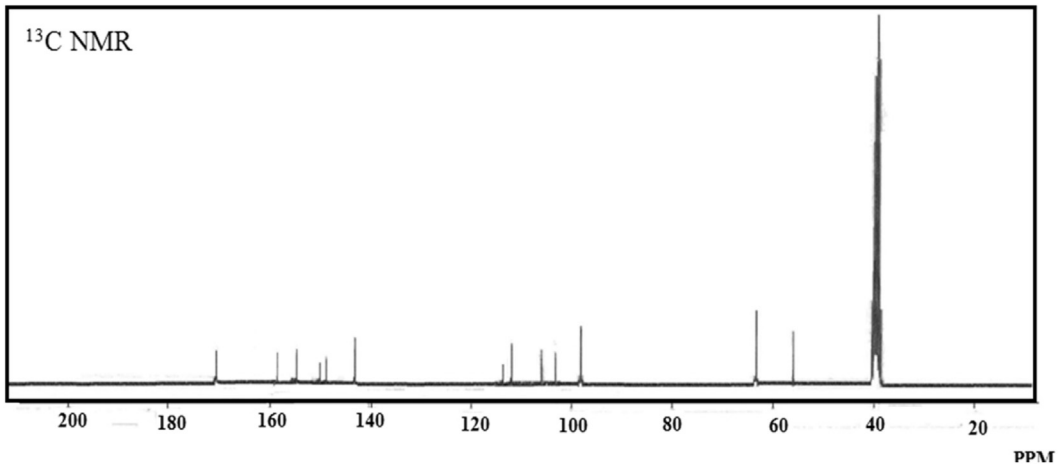

Fig. 5. The ^{13}C NMR spectrum of **HMOFCC**.

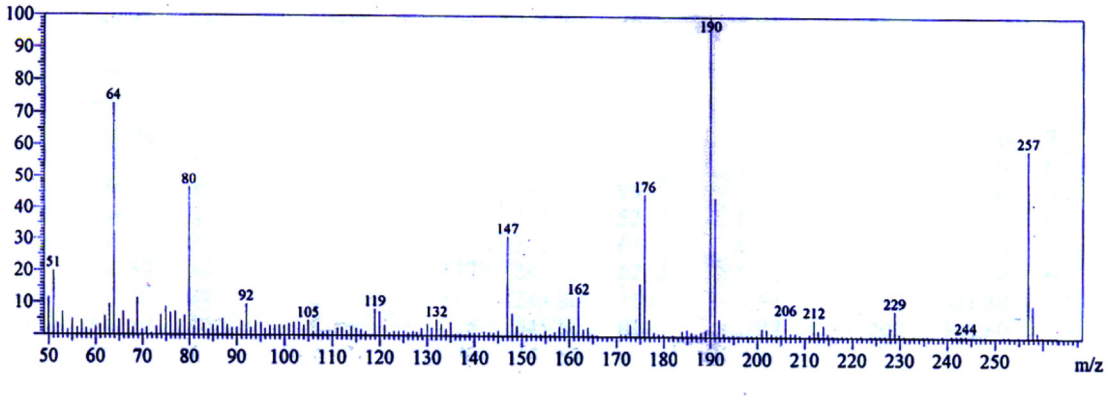

Fig. 6. The mass spectrum of **HMOFCC**.

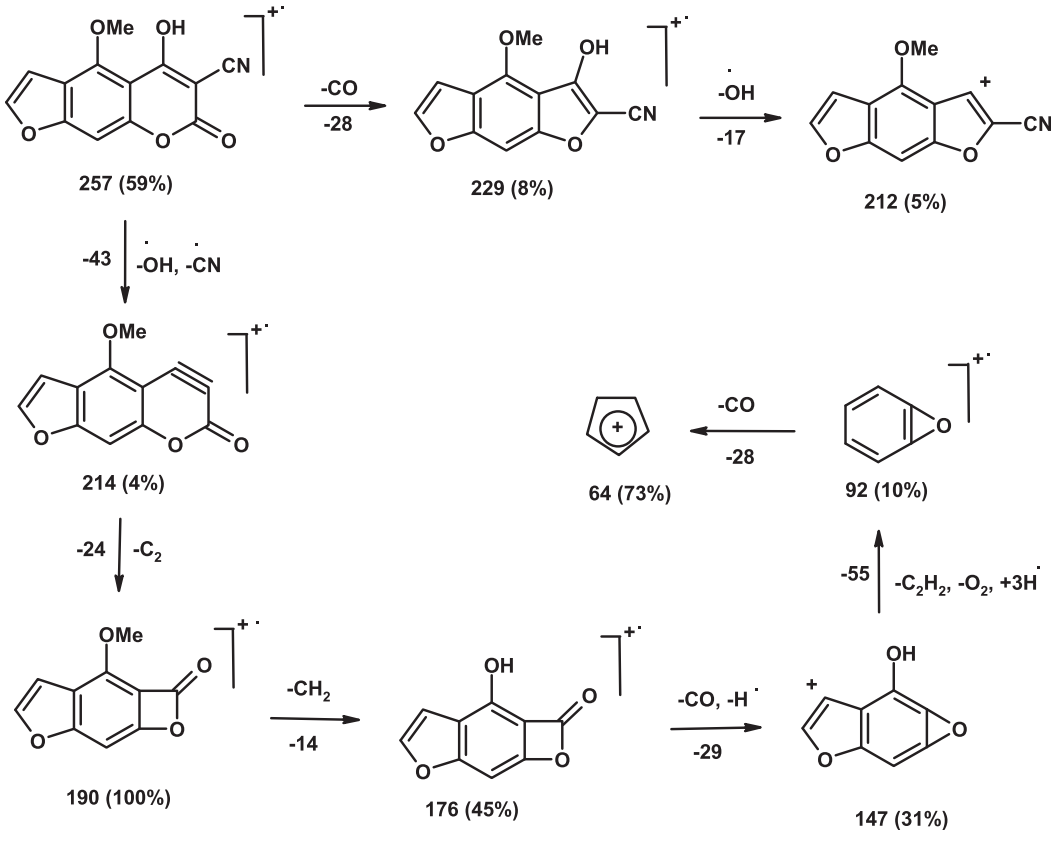

Fig. 7. The mass fragmentation pattern of **HMOFCC**.

distilled water (5 mL), was added with continuous stirring. The mixture of the reaction was warmed under reflux for 2 h. The yellow crystals obtained after cooling were filtered off and crystallized from ethanol to give compound **4** (**HMOFCC**) as pale yellow crystals, yield (0.38 g, 74%), m.p. 235-236 °C. IR (KBr, cm^{-1}): 3440 (OH), 3221 (CH_{furan}), 3003 ($CH_{arom.}$), 2928 ($CH_{aliph.}$), 2219 (C≡N), 1740 ($C{=}O_{\alpha\text{-pyrone}}$), 1622 (C=C). ^1H NMR (300 MHz, DMSO-d_6): 3.87 (s, 3H, OCH_3), 6.82 (s, 1H, H-9), 7.19 (d, 1H, H-3_{furan}, $J = 2.4$ Hz), 7.90 (d, 1H, H-2_{furan}, $J = 2.1$ Hz). ^{13}C NMR (75 MHz, DMSO-d_6): 56.2 (OCH_3), 63.6 (C-6), 98.1 (C-9), 102.8 (C-4a), 107.9 (C-3), 113.4 (C-3a), 115.8 (C≡N), 144.1 (C-9a), 149.5 (C-4), 151.8 (C-8a), 156.3 (C-2), 158.6 (C-7 as C=O), 171.3 (C-5). Mass spectrum (*m/z*, *I* %): 257 (M^+, 59), 229 (8), 212 (5), 190 (100), 176 (45), 162 (12), 147 (31), 119 (8), 92 (10), 80 (47), 64 (73). Anal. Calcd for $C_{13}H_7NO_5$ (257.19): C, 60.71; H, 2.74; N, 5.45%. Found: C, 60.50; H, 2.60; N, 5.20%. .

Melting points were determined on a digital Stuart SMP3 apparatus. The infrared spectrum was measured on FTIR Nicolet IS10 spectrophotometer (cm^{-1}), using KBr disk. ^1H NMR (300 MHz) and ^{13}C NMR (75 MHz) spectra were measured on Mercury-300BB, using DMSO-d_6 as a solvent and TMS (δ) as the internal standard. Mass spectrum was acquired utilizing the instrument type GC-2010 Shimadzu Gas chromatography instrument mass spectrometer (70 eV). Elemental microanalysis was performed Perkin-Elmer 2400II at the Chemical War Department, Ministry of Defense, Egypt.

2.1.1. Solvents

Two solvents were used (polar (methanol) and nonpolar (dioxane)) with AR-grade without further purification.

2.1.2. Apparatus

A Perkin-Elmer Lambda 4B spectrophotometer using 1.0 cm fused quartz cells was used to measure the electronic absorption spectra. The machine records linearly the percent of transmittance over the range 200–900 nm.

2.2. Thin film preparation and physical characterizations of ***HMOFCC***

Thin **HMOFCC** films were prepared on thermal vacuum evaporation model Edward Auto 306 for achieving a best effective and high-quality films. Full detailed information about the preparation conditions was described in details elsewhere by our group worker. Thermal characterization was made by using the Shimadzu-50H thermal analyzer. The operating heating temperature range is 20–800 °C with heating rate of 10 °C/min and a pure nitrogen

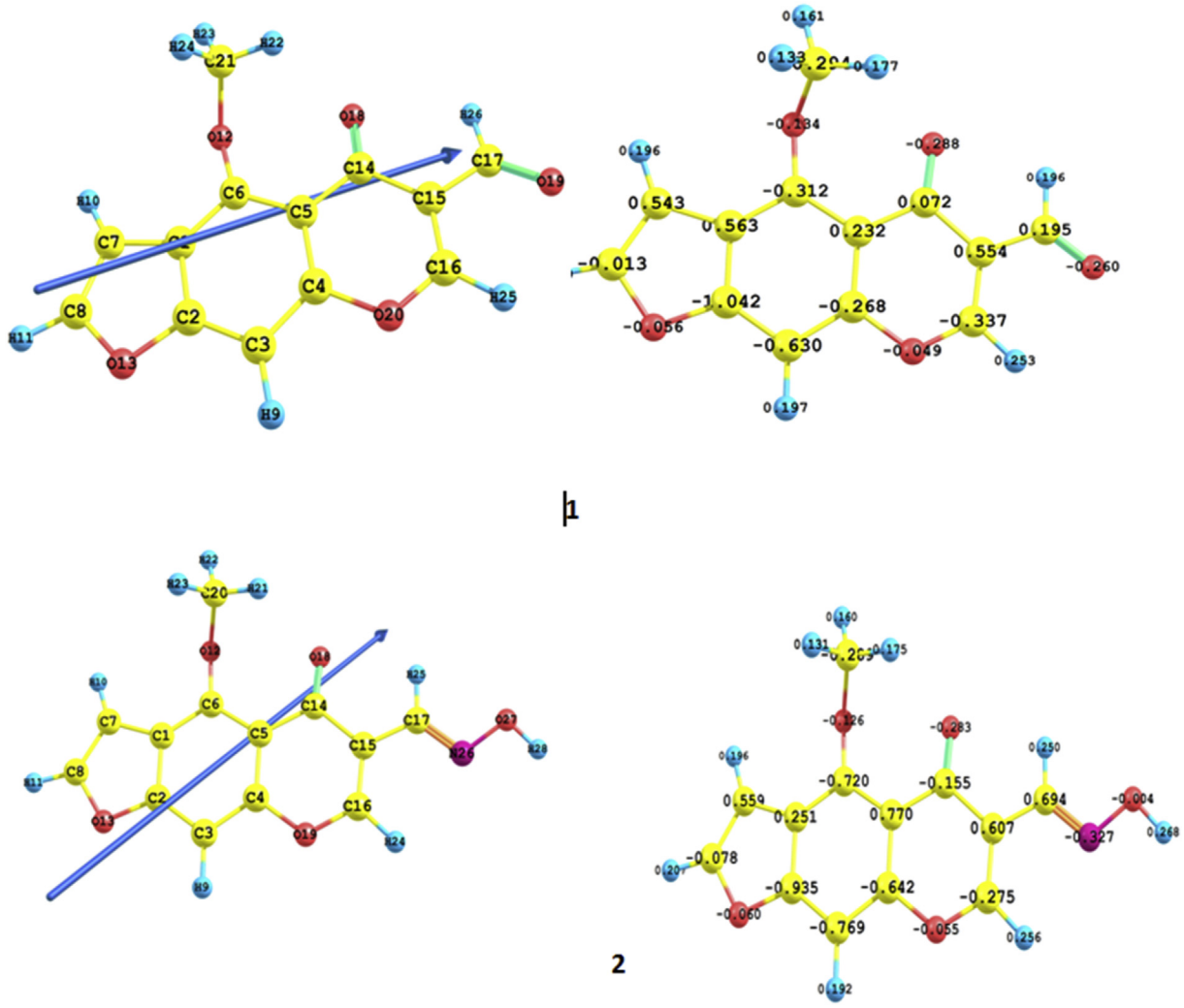

Fig. 8. Optimized geometry, numbering system, net charge, and vector of dipole moment for 4-methoxy-5-oxo-5H-furo[3,2-g]chromene-6-carboxaldehyde (**1**) and oxime(**2**) using B3LYP/6-311++G**.

atmosphere flow rate of 20 ml/min.

In addition, Scanning electron microscopy type JEOL-JSM-636 OLA was employed for surface morphology identification of **HMOFCC** samples. Spectral analysis of transmittance and reflectance in the wavelength range of 200–2500 nm were measured by JASCO– 670 spectrophotometer. Fluorescent spectra characteristic were achieved by Cary Eclipse fluorescence spectrophotometer. Current-voltage characteristics in dark and under various illumination intensities of 20–100 mW/cm^2 were measured by using type Keithly 2635 A and the input light was measured by using solar power meter type TM-206.

2.3. Computational methods

Calculations have been performed using Khon-Sham DFT (KS-DFT) method subjected to the gradient-corrected hybrid density functional B3LYP method [27]. The Becke's three parameters function is a combination of non-local exchange potential with the non-local correlation functional of Lee et al. [28]. Full geometrical optimization for each structure was performed using this function [28] and the 6-311++G(d, p) basis set [29] as implemented by Gaussian 09 package [30]. All geometries were visualized either using GaussView 5.0.9 [31] or chem craft 1.6 [32] software packages. During the geometry optimization, no symmetry constraints were applied.

3. Results and discussions

3.1. Molecular structure and reaction confirmation

In the present work, the reactivity of 6-formyl-visnagin (4-methoxy-5-oxo-5*H*-furo[3,2-*g*]chromene-6-carboxaldehyde) (**1**) was considered towards hydroxylamine hydrochloride. Thus, boiling carboxaldehyde **1** with hydroxylamine hydrochloride in acetic acid did not give either oxime **2** or carbonitrile **3**. Characterization of the spectral data cleared that, the isolated product was identified as 5-hydroxy-4-methoxy-7-oxo-7*H*-furo[3,2-*g*]chromene-6-carbonitrile (**HMOFCC)** (Fig. 1). This study revealed the existence of ring-opening ring-closure (RORC) reaction of γ-pyrone ring upon treatment with hydroxylamine hydrochloride. The formation of the unexpected product **4** may be explained if we considerate that two molecules of hydroxylamine reacted with aldehyde **1**, leading to the non-isolable oxime **2** which dehydrated to the non-isolable carbonitrile **3**. The intermediate **3** is highly active cyclic push-pull system that quickly add another molecule of hydroxylamine at C-7 giving the adduct **A**, followed by ring opening forming oxime **B** which in equilibrium in a ring-chain tautomerism. The oxime tautomer **B** dehydrated to produce malononitrile intermediate **C**, which underwent an intramolecular 6-*exo*-dig cyclization produced 7-iminofurocbenzopyrane intermediate **D** which upon hydrolysis furnished the final product (**HMOFCC)** (Fig. 2). The structure of compound (**HMOFCC)** was elucidated from

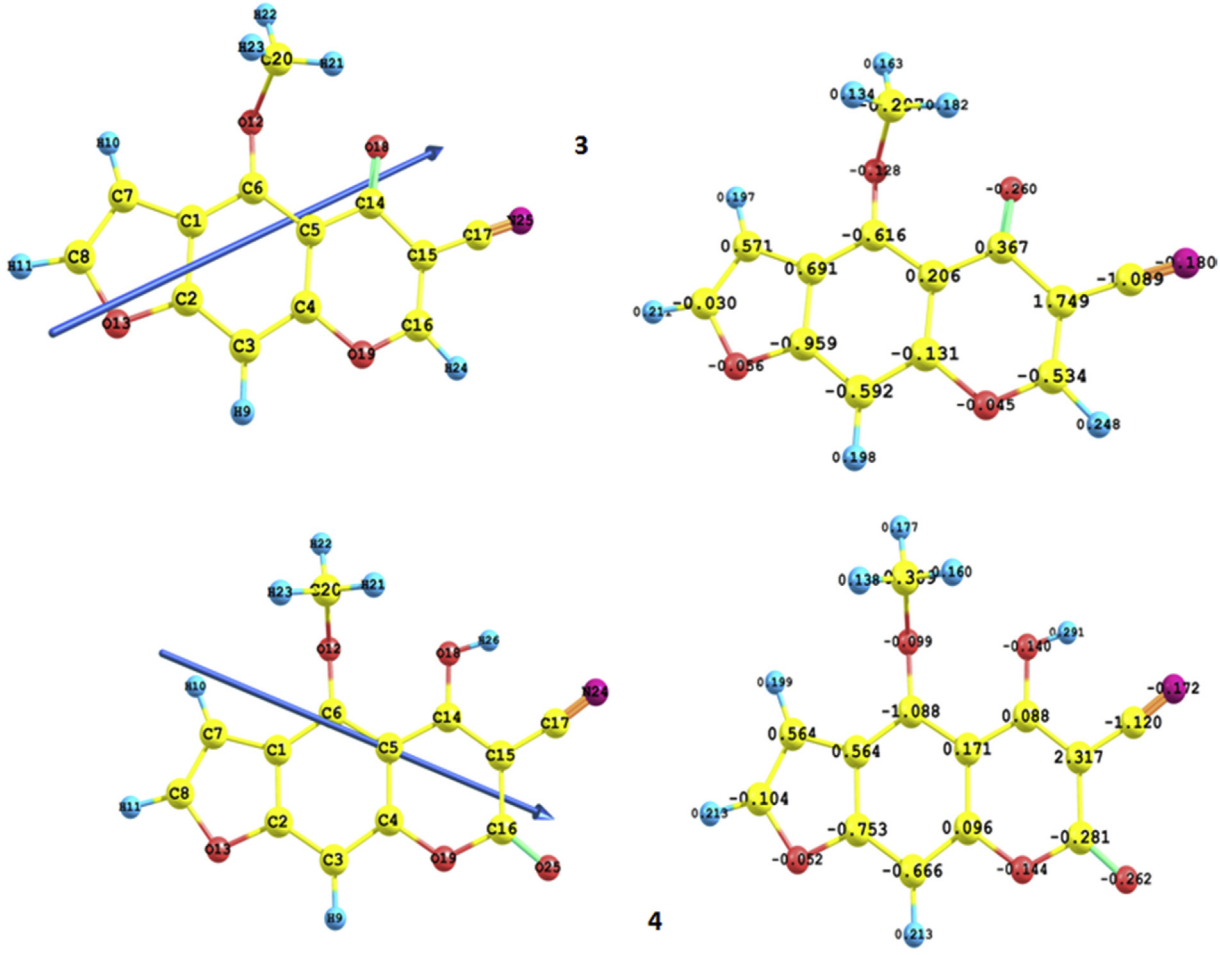

Fig. 9. Optimized geometry, numbering system, net charge, and vector of dipole moment for carbonitrile **3** and the product; 5-hydroxy-4-methoxy-7-oxo-7H-furo[3,2-*g*]chromene-6-carbonitrile (**HMOFCC**) using B3LYP/6-311++G**.

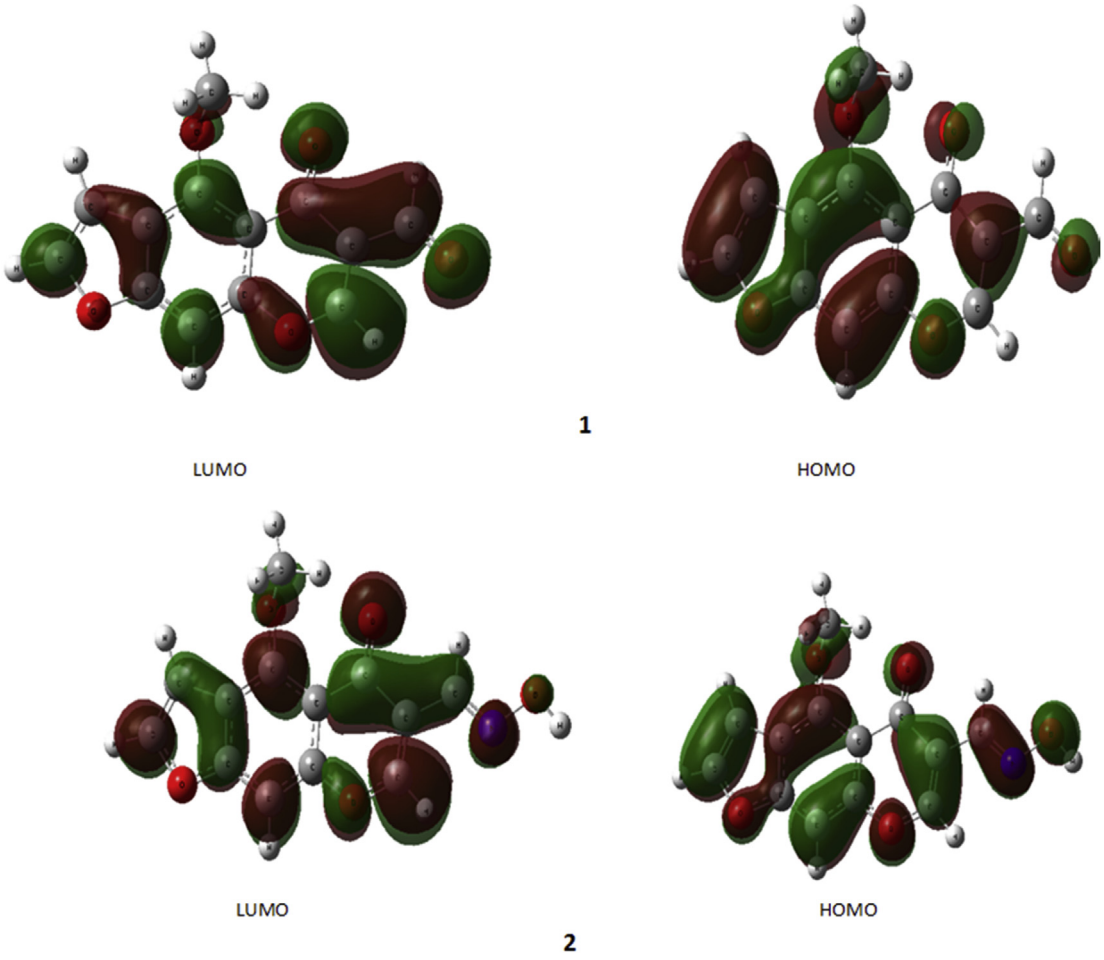

Fig. 10. HOMO and LUMO of carboxaldehyde **1** and the corresponding oxime **2**.

the interpretation of its spectral data. The IR spectrum (Fig. 3) showed characteristic absorption bands at ν_{max} 3440 (OH), 3221 (CH_{furan}), 3003 ($CH_{arom.}$), 2928 ($CH_{aliph.}$), 2219 (C≡N), 1740 ($C{=}O_{\alpha\text{-}pyrone}$), 1622 (C=C). Its ^{1}H NMR spectrum (Fig. 4) consists of two singles at δ 3.87 (OCH_3) and 6.82 (H-9) and two doublets at δ 7.19 and 7.90 assigned to H-3_{furan} and H-$2_{furan,}$ respectively. The ^{13}C NMR of compound **4** (Fig. 5) revealed signals equal to the total numbers of carbon atoms and agrees well with the suggested structure. Furthermore, the structure of compound **4** was deduced from its mass spectrum (Fig. 6) which revealed the molecular ion peak at *m/z* 257 which agrees well with its suggested molecular formula ($C_{13}H_7NO_5$) and supports the identity of the structure. The mass fragmentation pattern of **HMOFCC** compound is depicted in Fig. 7.

3.2. Molecular orbital calculations of the ground state energy

DFT calculation at the B3LYP level of theory and 6-311++G(d,p) as a basis set can be used to explain why the formation of the unexpected product (**HMOFCC)** is favored over the other products (oxime **2** and carbonitrile **3**).

The optimized structures of the studied compounds are obtained using the B3LYB/6-311++G(d,p) level, numbering system, net charge, a vector of dipole moment, and the charge density maps of HOMO and LUMO are presented in Figs. 8–11. The total energy (E_T), the energy of highest occupied molecular orbital (E_{HOMO}), the energy of lowest unoccupied molecular orbital (E_{LUMO}), energy gap (E_g) and the dipole moment (μ) of all compounds are presented in Table 1. The analysis of Table 1 and Figs. 8–11 shows that:

The most stable geometry of the studied compounds, **1-4**, is the planar structures as indicated from the dihedral angles. From the calculations of the energy gap, (E_g), which measure the chemical activity, compound **4** was found to be more reactive than compounds **2** and **3** by 0.0218 and 0.1221 eV (≈1 and ≈ 3 kcal), respectively (Table 1). Accordingly, one can put the order of decreasing the energy gap (E_g) is **3** > **1** > **2** > **4**. The polarity or charge separation over the molecule, which is measured by the dipole moment (μ) showed that; (μ) of compound **4** > (μ), of compounds **2** and **3** by 5.27 and 1.44 D, respectively. Also, the vector of the dipole moment of compound **4** in opposite direction of the vector (μ) of compounds **2** and **3**. So, the general trend of the dipole moment (μ), for the studied furobenzopyrone derivatives follows the order **4** > **3** > **1** > **2**. Based on these results; the formation of the unexpected product **4** is attributed to two molecules of hydroxylamine step-wisely reacted with aldehyde **1**, leading to the non-isolable oxime **2** which dehydrated to the non-isolable carbonitrile **3** as shown in Fig. 1.

Another reason which may explain the stability of compound **4** is the localization of all the charge density of the HOMO on benzofuran moiety more than the other moiety (Fig. 11) in contrast to compounds **2** and **3** where the charge density of the HOMO is delocalized over all the molecule (Fig. 10). In addition, another reason for the formation of compound **4** is the Mullikan electron density which supports the proposed mechanism described in

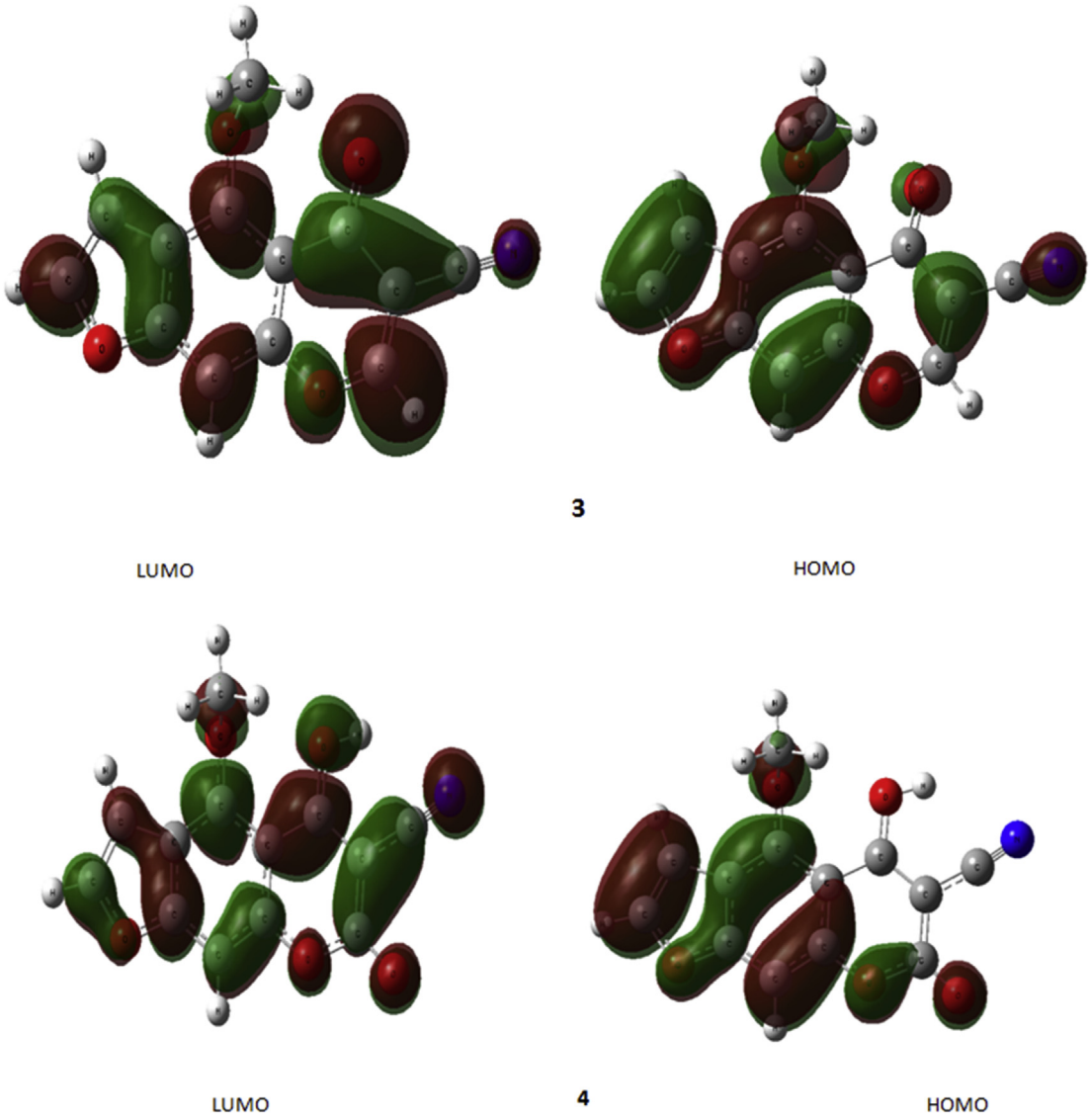

Fig. 11. HOMO and LUMO of carbonitrile **3** and the product; 5-hydroxy-4-methoxy-7-oxo-7H-furo[3,2-g]chromene-6-carbonitrile (**HMOFCC**).

Table 1
Total energy, energy of HOMO and LUMO, energy gap and dipole moment of 5-hydroxy-4-methoxy-7-oxo-7H-furo [3,2-g]chromene-6-carbonitrile (**4, HMOFCC**) and the studied compounds computed at the B3LYP/6-311++G(p,d) level of theory.

Parameters	1	2	3	4
E_T (au)	−876.505	−931.827	−855.411	−930.681
E_{HOMO} (eV)	−6.5993	−6.2623	−6.6969	−6.8416
E_{LUMO} (eV)	−2.4069	−2.1246	−2.4589	−2.7257
E_{gap} (eV)	4.1923	4.1377	4.2380	4.1159
μ (Debye)	5.45	3.39	7.22	8.66

Fig. 1. The electron density concentrated at C-15 of compound **4** more than expected compounds **2** and **3**; i.e. the electron density at C-15 in compound **4** is equal to 2.317 but the electron density at the same position C-15 in compounds **2** and **3** is equal to 0.607 and 1.749, respectively (Figs. 8 and 9). These results confirm the high nucleophilicity of C-15 in the α-pyrone ring and support the suggested mechanism depicted in Fig. 1. The computed ionization energy (I.E.) of compound **1** which measures the donating property (oxidation power) is found to be 6.60 eV as listed in Table 1.

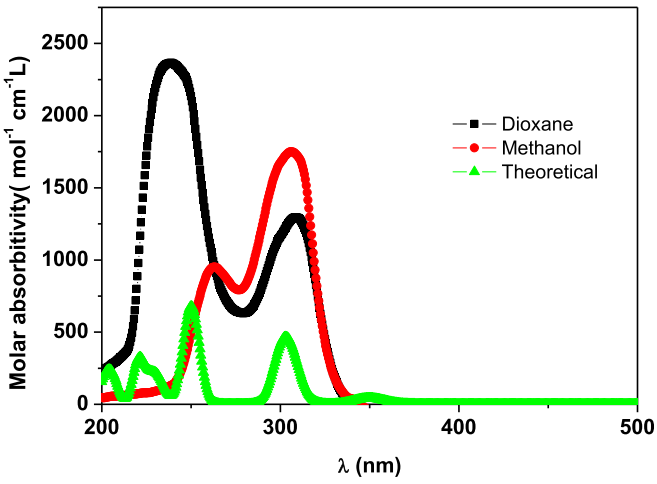

Fig. 12. Electronic absorption spectra of **HMOFCC**.

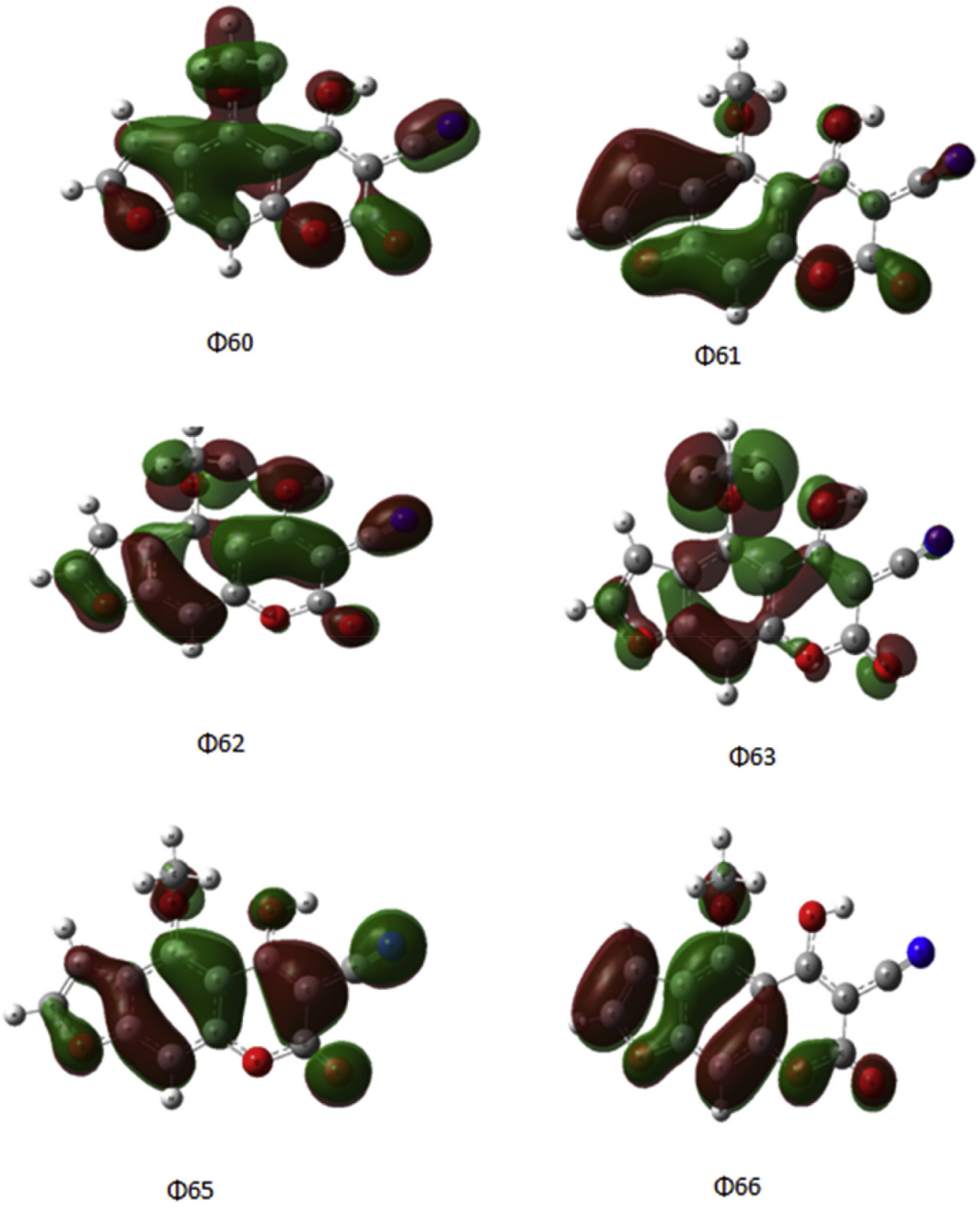

Fig. 13. The charge density maps of the occupied of **HMOFCC**.

Introducing a C═N-OH and CN- groups in compounds **2**-**4** showed a significant change in the I.E. and hence in the donating properties. So; the order of decreasing the donating power is **2** > **1** > **3** > **4**. However, the electron affinity (E.A) of **1** which measures the accepting property (reducing power) is 2.41 eV. The order of accepting properties of furor benzopyrone derivatives follows **2** < **1** < **3** < **4**.

3.3. Electronic absorption spectra of the novel compound (*HMOFCC*)

The electronic absorption spectra, in nonpolar (dioxane) and polar (methanol) solvents, are presented in Fig. 12. The charge density maps of the occupied and vacant MO's considered in the transitions is presented in Figs. 13 and 14. The comparison between the experimentally and theoretically computed spectra is listed in Table 2. As observed, the spectrum, in dioxane, possesses three main band systems. Two bands are found for the long wavelength centered at 343 and 308 nm, while the medium envelope composed of two bands centered at 260 and 239.7 nm. The third band is made out of two bands focused at 223.6 and 209 nm. Increasing solvent polarity causes a blue shift of all observed bands. Furthermore, the intensity of the bands is found to increase as a result of increasing the polarity of the solvent. All the observed bands may be attributed to π-π^* transitions as reflected from their intensities (100-2500). Excited configurations, considered in this work, are those resulted from an electron excitation between the highest six occupied molecular orbital's Φ_{60}-Φ_{66} and the lowest six unoccupied molecular orbital's Φ_{67}-Φ_{74}. The configuration interaction matrix is solved and the configuration interaction state

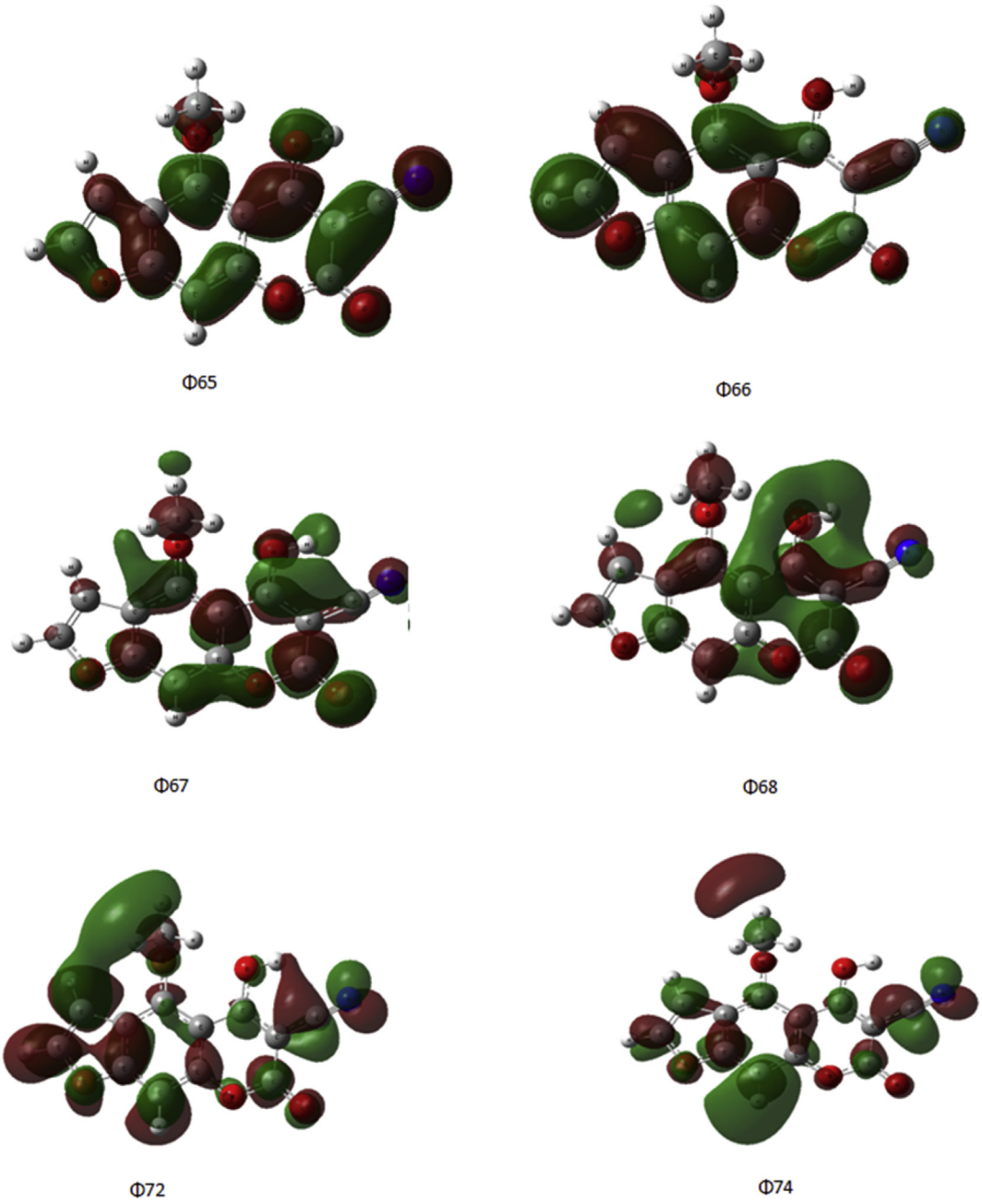

Fig. 14. The charge density maps of the unoccupied of **HMOFCC**.

functions are tabulated in Table 2. The long wavelength absorption band has been computed theoretically at 349.74 nm and composed of two configurations, namely, $\varphi^{-1}_{65}\ \varphi_{68}$ and $\varphi^{-1}_{66}\ \varphi_{67}$. The configuration $\varphi^{-1}_{65}\ \varphi_{68}$ is delocalized whereas; $\varphi^{-1}_{66}\ \varphi_{67}$ is localized transitions. The second $(\pi, \pi^*)^1$ state-centered, is computed theoretically at 303.06 nm in agreement with the experimentally observed values. This state is composed of two configurations, namely, $\varphi^{-1}_{65}\ \varphi_{67}$ and $\varphi^{-1}_{66}\ \varphi_{68}$ and possesses the same polarity as the ground state. Hence, show no pronounced solvent effect. The third $(\pi, \pi^*)^1$ state computed theoretically appears at 250.79 nm and composed of five configurations, namely, $\varphi^{-1}_{60}\ \varphi_{67}$, $\varphi^{-1}_{62}\ \varphi_{67}$, $\varphi^{-1}_{65}\ \varphi_{67}$, $\varphi^{-1}_{65}\ \varphi_{68}$ and $\varphi^{-1}_{66}\ \varphi_{68}$. A blue shift in this band was observed on increasing solvent polarity i.e. solvent dependent. This is might be ascribed to the moderately high polarity of the excited state as compared to that of the ground state. These states may be assigned as a delocalized and localized transition. The fourth $(\pi, \pi^*)^1$ state is computed theoretically at 247.06 nm. This state is composed of five configurations, namely, $\varphi^{-1}_{62}\ \varphi_{67}$, $\varphi^{-1}_{65}\ \varphi_{68}$, $\varphi^{-1}_{66}\ \varphi_{68}$, $\varphi^{-1}_{66}\ \varphi_{69}$ and $\varphi^{-1}_{66}\ \varphi_{70}$. This state shows no solvent dependence and assigned as a delocalized and a charge transfer band (CT) from benzofuran to the α-pyrone moiety. The fifth $(\pi, \pi^*)^1$ state theoretically calculated at at 220.54 nm and found to be composed of five configurations, (see Table 2). The last one state is theoretically computed appears at 204.64 nm and assigned as a delocalized and localized transitions (see Table 2).

3.4. Thermal analysis characterization

The thermal immutability of the material is substantial to be examined for manufacturing any thin films application. The

thermal characteristics of HMOFCC were achieved through thermogravimetric analysis (TGA) at the heating rate of 20 °C min^{-1} under the atmosphere of nitrogen gas in the temperature range of 50–750 °C and illustrated in Fig. 15. The thermogram showed the highest onset peak centered at ~335 °C with highest weight loss corresponding to the melting point of the structure. Accordingly, the presented structure showed thermal stability up to 335 °C, in good agreement with those measured by SMP3. The presented thermal stability under high temperature gives good significance for thin films and solar cell fabrication.

3.5. Surface morphology characterization

The surface morphology of **HMOFCC** samples was produced using SEM images with low and high magnifications as shown in Fig. 16(a–c). It can be seen that the particles are irregular in its shape and sizes but an interesting results for the higher magnification images is presented. A cauliflower-like, as well as, needle-like leaves structures were the resulting morphology from observed images. Furthermore, agglomerated of the prepared nanoparticles structures were also obtained. The mean particle size was obtained by using particle size analyzer and found to be 450 nm.

3.6. Photoluminescence characterization

The room temperature photoluminescence spectra (PL) of **HMOFCC** samples using wavelength excitation of 300 nm in different solutions are shown in Fig. 17. As can be expected, a red-shift for the characteristic emission peak that is consistent with the solvent type. The observed characteristic peaks are recorded for the structure in a solvent of methanol, ethanol, DMF, benzene, and acetone at 410, 426,445,461 and 480, respectively. The intensity, broadening and the position of the peaks are dependent on the solvent type. The obtained results are in agreement with those published for one of the chromene derivative (**BOCTIX**) [33].

3.7. Optical characterizations of *HMOFCC* thin films

Ganesh et al. [34] stated that the study of the optical characteristics of both direct and/or indirect band gap materials give a big significance owing to their applicability for optoelectronic devices. The spectral dependence of $T(\lambda)$ and $R(\lambda)$ for the HMOFCC films is shown in Fig. 18. As observed, the summation of $T(\lambda)$ and $R(\lambda)$ in the non-absorbing region (at $\lambda \geq 800$ nm) is nearly equal to unity. At shorter wavelength region (absorbing region, at $\lambda \leq 800$ nm) the summation of $T(\lambda)$ and $R(\lambda)$ is lower than unity due to the light absorption. The presence of the transmission band in the spectral region of 350–600 nm confirms that the **HMOFCC** films are suitable for application as optical filters [35].

The optical band gap (E_g) of the material can easily be estimated from the analysis of the high intense variation of optical absorption region nearby the fundamental absorption edge. The absorption coefficient (α) can be obtained from the following expression [36];

$$\alpha = \frac{1}{d}\ln\left(\frac{(1-R)^2}{2T} + \left(\frac{(1-R)^4}{4T^2} + R^2\right)^{1/2}\right) \quad (1)$$

Table 2
Calculated band maxima and intensities of **HMOFCC** by TD method.

State	Theoretical				Type	Experimental	
	Configuration	Coefficient	λ, nm	*f*		Polar	Non- polar
						λ, nm	λ, nm
I	65–68 66–67	−0.1034 0.69426	349.74	0.0314	π–π*	–	–
II	65–67 66–68	0.67572 0.15275	303.06	0.3462	π–π*	306.07	308.06
III	60–67 62–67 65–67 65–68 66–68	−0.10042 0.22151 −0.13376 0.38684 0.49395	250.79	0.4152	π–π*	253.07	260.02
IV	62–67 65–68 66–68 66–69 66–70	−0.13874 0.52480 −0.37251 −0.16824 0.10789	247.06	0.1207	π–π*	–	–
V	61–67 62–68 65–68 66–69 66–70	0.16783 0.12087 −0.18159 −0.30761 0.53012	220.54	0.2083	π–π*	–	–
VI	60–67 61–68 62–67 63–68 65–69 65–70 66–72 66–74	0.10336 0.16900 0.13321 0.23366 0.29272 0.31573- 0.37835 −0.10605	204.64	0.0754	π–π*	–	–

The interband absorption coefficient for a direct allowed transition has a relation with the photon energy according to the following formula [37].

$$\alpha(h\nu) = A(h\nu - E_g)^{1/2} \quad (2)$$

where A is a characteristic constant parameter. Fig. 19 shows the plots of $(\alpha h\nu)^2$ as a function of photon energy ($h\nu$). This figure reveals a linear portion supporting the direct allowed transition and the intercept with x-axis at $(\alpha h\nu)^2 = 0$. Accordingly, the energy band gaps are found to be 1.16 and 2.56 eV, respectively for the onset and the fundamental energy band gap. The obtained energy gaps are in good agreement with the most published in the literature for the optical gaps of organic semiconductors [38–41]. The onset energy gap is referred to as the optical band gap or exciton level in solids but the highest one is referred to the transport gap [42]. The onset optical band gap is less than the fundamental energy gap and the variation can be attributed to the exciton binding energy which has a value of 1.40 eV. The obtained exciton binding energy is in agreement with those published in the literature [43,44].

The obtained optical band gap is suitable for the absorption of the solar spectrum in the application for organic solar cells, according to the reported in the literature by Costa et al. [45]. It is observed that the experimental energy gap is found to be significantly lower than those obtained from the theoretical one due to the fact that the theoretical calculations depend on the gas phase for isolated molecule [46].

There are many important dispersion parameters such as single oscillator energy, E_o, and the dispersion energy, E_d. These parameters can be estimated using the single oscillator model for the normal dispersion region expressed by Wemple-DiDomenico (WDD) as follows [47]:

$$\left(n^2 - 1\right)^{-1} = \left(\frac{E_0^2 - E^2}{E_0 E_d}\right) \quad (3)$$

Fig. 20(a) shows the plotting of $(n^2\text{-}1)^{-1}$ against E^2 for HMOFCC thin films. Values of E_0 and E_d can easily be determined from both the slope $(=\frac{1}{E_d E_0})$ and the intercept $(=\frac{E_0}{E_d})$. The calculated values of E_0 and E_d are found to be 4.08 and 27.14 eV. The obtained value of oscillator energy is in agreement with those determined for some organic thin films published elsewhere [48–50], but the obtained dispersion energy is higher than those published due to the high refractive index of **HMOFCC** films.

Another important dispersion parameter is the high-frequency dielectric constants, $\varepsilon\infty$, which can be easily determined using the following expression [51]:

$$n^2 = \varepsilon_\infty - \left(\frac{e^2 N}{\pi c^2 m^*}\right)\lambda^2 \quad (4)$$

where e is the electronic charge, c is the light speed, N is the carrier concentration, and m^* is electron effective mass. Fig. 20 (b)

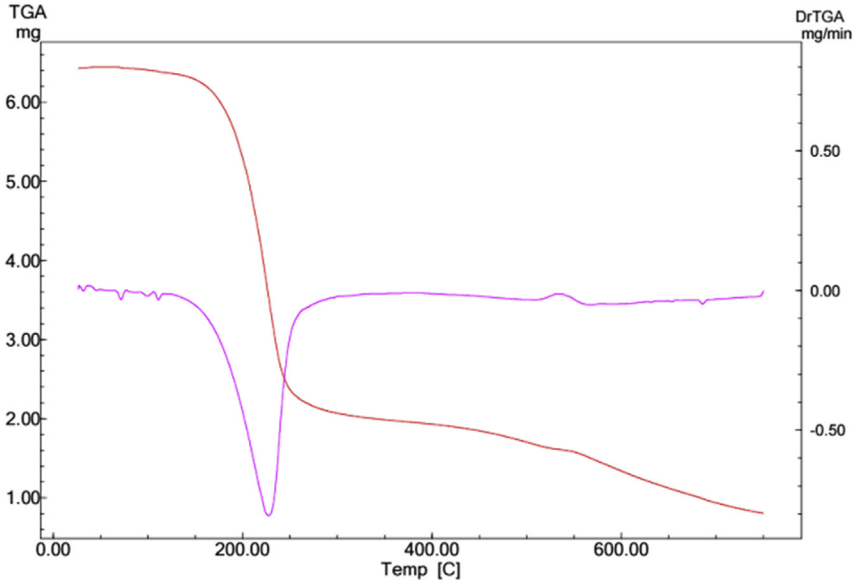

Fig. 15. TGA curves of powder **HMOFCC**.

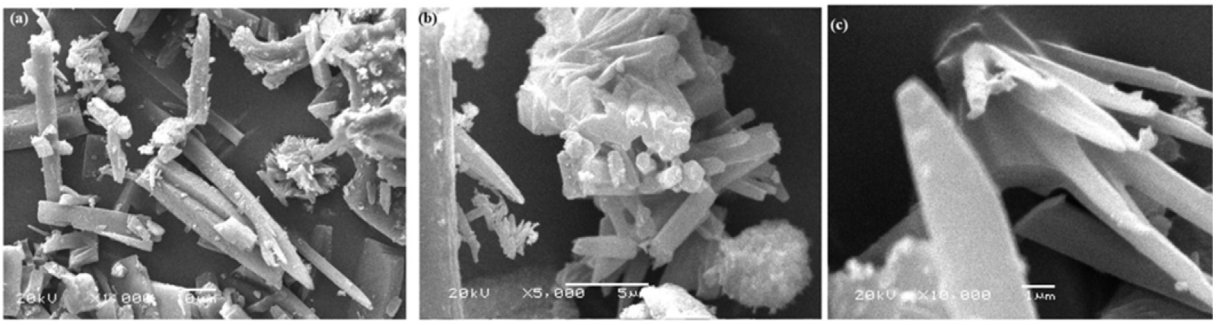

Fig. 16. SEM of different magnifications (a) 1000 x, (b) 5000 x, and (c) 10,000 x.

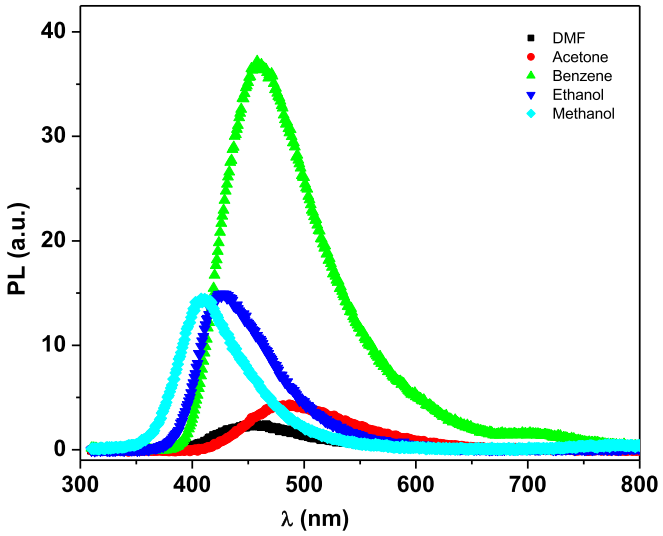

Fig. 17. PL characteristics of **HMOFCC** using different solvents.

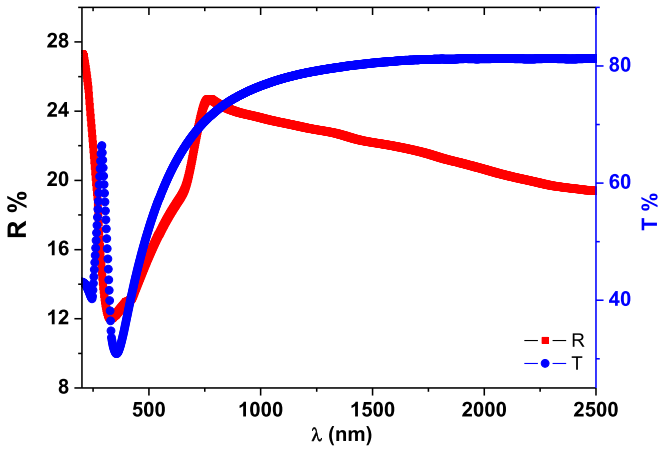

Fig. 18. Spectral dependence of T and R characteristics of **HMOFCC** thin films.

illustrates the plot of n^2 against λ^2 for HMOFCC thin films. It can be seen that the value of ε_∞ can be estimated from the extrapolation of the straight line fit to the y-axis and found to be 6.08 Furthermore, the ratio of N/m^* was estimated from the slope of the straight line and found to be 3.2×10^{56} m^{-3}/kg. These optical parameters are in agreement with those published for most of the organic thin films [52–55].

It is noted that the essential spectrum of excitation of electron of the material is correlated with the frequency-dependent of complex dielectric constant as reported by El-Nahass et al. [56] and Sarkar et al. [57]. Fig. 21 shows the spectral distribution of real, ε_1 and imaginary dielectric, ε_2 constants. As observed, the common feature is the higher values of ε_1 as compared with ε_2 at the same wavelength which gives the indication of the probability of various interactions are considered between the incident photons and the charge carriers in the film. In addition, El-Nahass et al. [56] have attributed the difference in the shape of the curves and the peak positions of ε_1 and ε_2 to the fact that ε_1 is related to the slowing down of light in a material, described by the refractive index, but ε_2 is apparently a measure of energy absorption or energy-loss. Other related parameters to the dielectric constant which defined as the real, σ_1, and the imaginary, σ_2, parts of the optical conductivity. These parameters enable to reveal any additional allowed interband optical transitions. The optical conductivity also refers to the conductivity of the material in the presence of an alternating electric field through the entire frequency range of the incident light. The relations for calculating these parameters were published elsewhere [58–60]. Fig. 22 shows the variation of the real, σ_1, and the imaginary, σ_2, parts of the optical conductivity spectral distribution of σ_1 and σ_2 for **HMOFCC** thin films in the desired wavelength. As observed from Fig. 22 that σ_1 is larger than σ_2 at the same wavelength. Moreover, there is a different behavior of the two parts of conductivity with wavelength.

3.8. Current density-voltage characteristics

The current density – voltage characteristics of **HMOFCC**/p-Si heterojunction in dark and under different illumination intensities in the range 20–100 mW/cm^2 is shown in Fig. 23. Obviously, the current under illumination is found to be higher than for dark and increases with increasing illumination intensity at the same applied

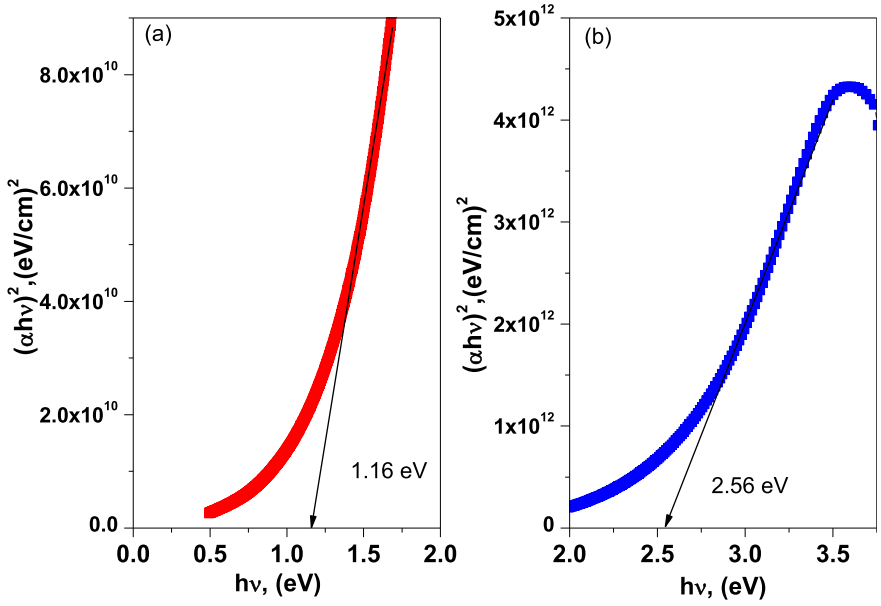

Fig. 19. Plot of $(\alpha h\nu)^2$ vs. hν of (a) region I and (b) region II for **HMOFCC** thin films.

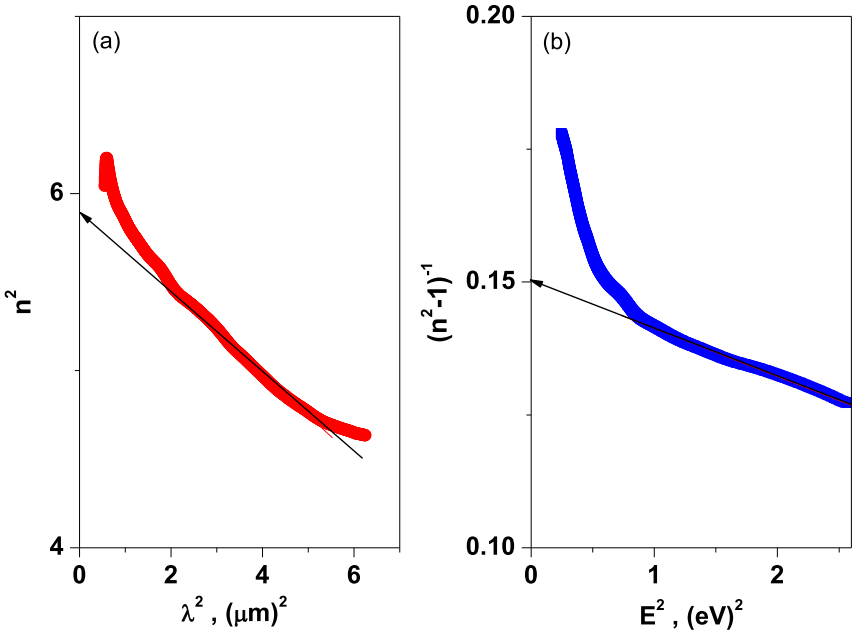

Fig. 20. (a) Plot of n^2 vs. λ^2 and (b) Plot of $(n^2\text{-}1)^{-1}$ vs. E^2 for **HMOFCC** thin films.

voltage. In addition, the current density-voltage characteristics under dark and illumination intensity show diode-like behavior and rectification characteristics. Sharma et al. [61] have suggested that the photocurrent generates due to the formation of exciton followed by dissociation to free charge carrier at the interface of the heterojunction. Therefore, an increase for the photocurrent as the light intensity increases. A re-plotting of the current density-voltage data, shown in Fig. 23, in a double logarithmic plot, shown in Fig. 24 (a) is taken place to study the predominant carrier conduction mechanisms. As observed, the plot displays two different distinct regions under dark and illumination conditions indicating the presence of two predominate conduction mechanisms. In the case of the region I, the slopes of all curves are found to be ~1, confirming that the predominant conduction mechanism is ohmic conduction and obeys Ohm's law [62]. This behavior can be ascribed to the considerable reduction of the injected carriers from the electrodes. But, in region II, the current displays power law exponent, i.e. $J\alpha V^m$ with slope (m) of about ~2 confirming that the

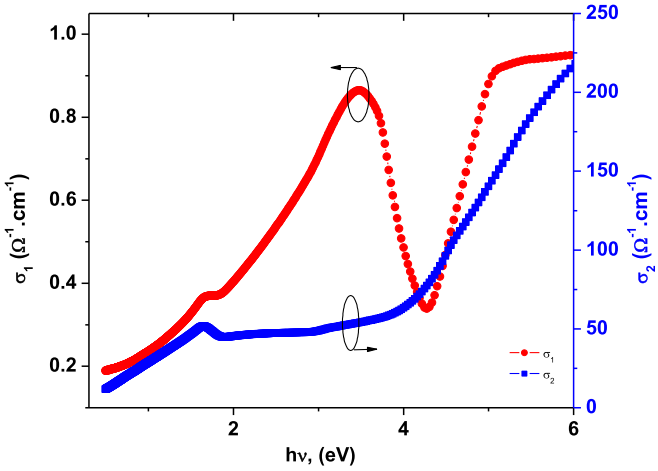

Fig. 22. (a) Plot of σ_1 vs. hν and (b) Plot of σ_2 vs. hν for **HMOFCC** thin films.

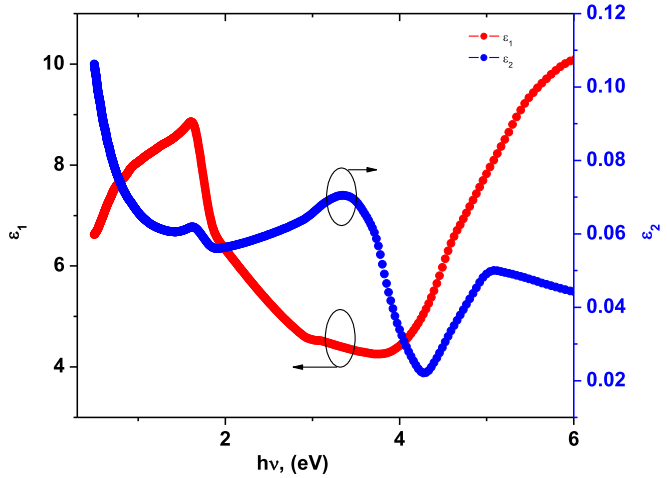

Fig. 21. (a) Plot of ε_1 vs. hν and (b) Plot of ε_2 vs. hν for **HMOFCC** thin films.

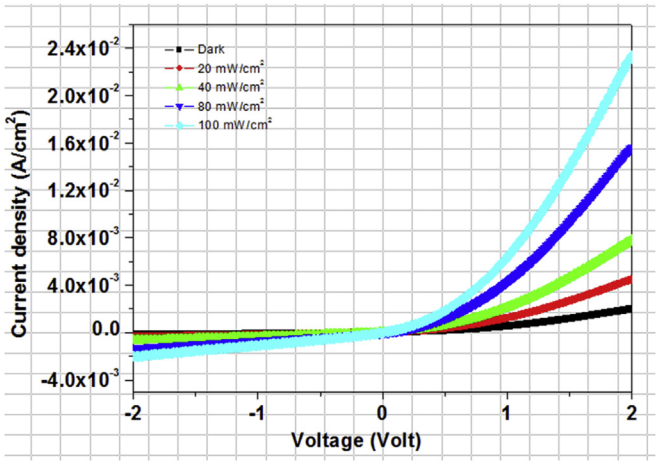

Fig. 23. Current density-voltage characteristics of **HMOFCC** thin films.

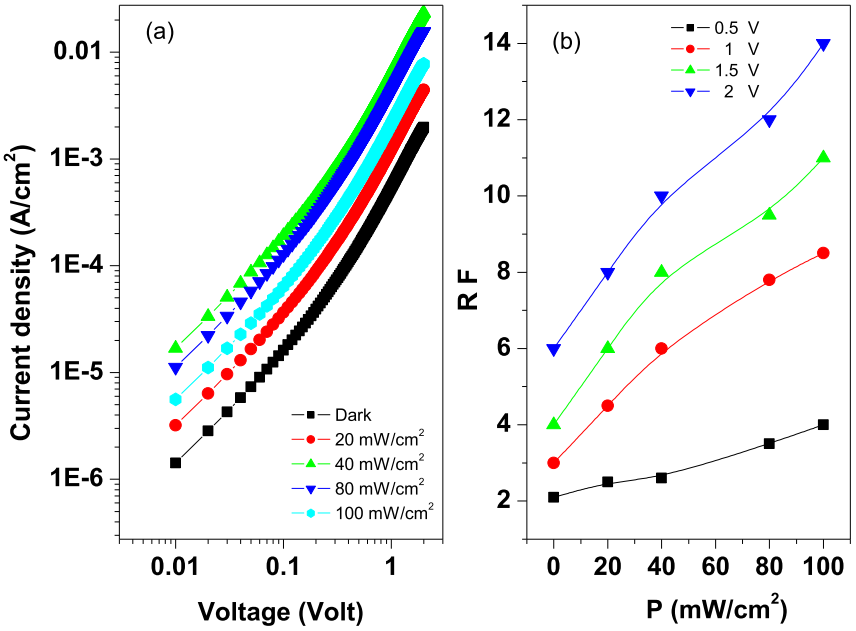

Fig. 24. (a) Plot of current density vs. Voltage and (b) Plot of RF vs. P for **HMOFCC** thin films.

current obeys space charge limited conduction, dominated by single trap [63]. In addition, Rectifying characteristics of the heterojunction can easily be clearly observed for the samples under dark and illumination conditions. Fig. 24 (b) shows the illumination intensity dependence of the rectification factor. As observed, an increase in the rectification factor with increasing the light intensity and decreasing applied voltage. This behavior gives an evidence for the enhancement of the heterojunction characteristics with increasing intensity of light [33].

Furthermore, there are important parameters such as the reverse saturation current, series and shunt resistances were considered in this study as a function of light intensity as shown in Fig. 25. As observed, an increase in the reverse saturation current with increasing light intensity due to lowering the barrier height of the heterojunction as light intensity increased. But series and shunt resistances are found to be decreased with increasing light intensity in the desired range. Decreasing of the series resistance as the light intensity increases gives another support for the enhancement of the heterojunction characteristics as the light intensity increases.

3.9. Transient photocurrent response under different light illuminations

To further study the characteristics of the heterojunction under different illuminations, phototransient current properties were studied as shown in Fig. 26. For this purpose, the heterojunction was prepared in a special hand-made chamber and the light is turning on and off for different times with different light intensities in the range 20–100 mW/cm^2. As observed from the Fig. 26, under shining of the light (on-state), a sharpness increase of photocurrent as a function of light intensity is recorded. After which, all curves attain to a stable zone for a certain time. When the light is turned off state, the photocurrents relax for a small time, followed by a sharpness decay and come back to approximately the origin value. Zhang et al. [64] and Guo et al. [65] have attributed this behavior to the presence of more surface states and defects which have the ability for catching the photogenerated carriers and diminish the charge separation performance.

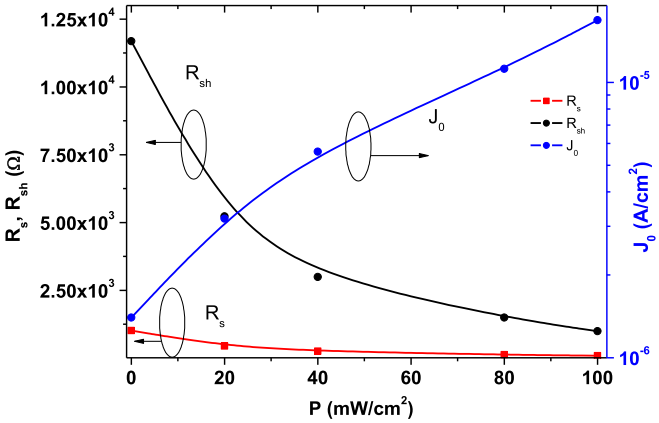

Fig. 25. (a) Plot of R_s, R_{sh} and J_0 vs. P for **HMOFCC** thin films.

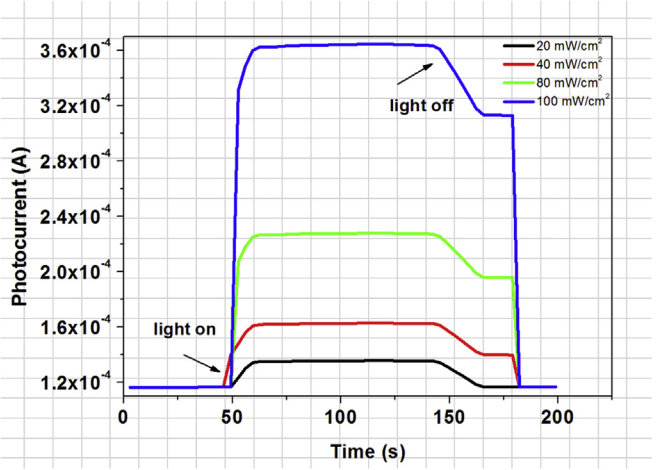

Fig. 26. Plot of photocurrent vs. Time for **HMOFCC** thin films.

4. Conclusion

The structure of the synthesized **HMOFCC** was emphasized on the basis of various spectral data of IR,^{1}H NMR,^{13}C NMR and mass spectra. The molecular geometry of **HMOFCC** in the ground state was achieved by using DFT-B3LYP/6-311++G (d,p) level of theory. The optimized structure is planar as indicated from the dihedral angles. Mulliken and natural charge distribution indicated the electronic charge distribution in the structure. All the observed bands in the UV spectrum were assigned to π-π^* transitions as reflected from their intensities. The agreement between the theoretically computed and the experimentally observed transitions are satisfactory. The solvent dependence of the observed bands was attributed to the change in the transition dipole moments of the ground and excited states. Two direct optical gaps were extracted from the analysis of the absorption coefficient at the optical band edge and found to be 1.16 and 2.56 eV. The main important optical parameters like, E_0, E_d and ε_∞ are found to be 4.08, 27.14 eV and 6.08, respectively. The current under illumination is found to be higher than for dark at the same voltage and increases with increasing illumination intensity at the same applied voltage for **HMOFCC**/p-Si heterojunction. The reverse saturation current of the heterojunction increases with increasing light intensity due to lowering the barrier height. A remarkable increase of photocurrent of the heterojunction as a function of light intensity supports the applicability of the studied heterojunction for the photodiode devices.

References

[1] A.A. Abu-Hashem, M. El-Shazly, Eur. J. Med. Chem. 90 (2015) 633–665.
[2] R.B. Gammill, C.E. Day, P.E. Schurr, J. Med. Chem. 26 (1983) 1672–1674.
[3] D. Vedaldi, S. Caflleri, F. Dall'Acqua, L. Andrea, L. Bovalini, P. Martelli, Farmaco 4 (1988) 333–346.
[4] L. Trabalzini, P. Martelli, L. Bovalini, F. Dall'Acqua, E.J. Sage, Photochem. Photobiol. B Bio. 7 (1990) 317–336.
[5] M. Ghate, M.V. Kulkarni, Indian J. Chem. 44B (2005) 1674–1678.
[6] M.S. Frasinyuk, S.V. Gorelov, S.P. Bondarenko, V.P. Khilya, Chem. Heterocycl. Comp. 45 (2009) 1261–1269.
[7] A.A. Abu-Hashem, M.M. Youssef, Molecules 16 (2011) 1956–1972.
[8] I.F. Zaeid, A.M. Nasef, N.M. Fawzy, A.M. Soliman, M.M. El-Baroudy, Int. J. Pharm. Sci. Rev. Res. 30 (2015) 306–314.
[9] H. Regaila, A. Gohar, G. Abdel Sadek, Egypt. J. Pharm. Sci. 29 (1988) 343–348.
[10] F. Eiden, G. Radenmacher, J. Schuenemann, Arch. Pharm. 316 (1984) 539–547.
[11] M.A. Ibrahim, T.E. Ali, A.M. El-Kazak, A.M. Mohamed, Heterocycles 50 (2013) 1075–1086.
[12] M.A. Ibrahim, N.M. El-Gohary, Heterocycles 89 (2014) 413–425.
[13] M.A. Ibrahim, T.E. Ali, A.M. El-Kazak, A.M. Mohamed, J. Heterocycl. Chem. 52 (2015) 815–826.
[14] M.A. Ibrahim, T.E. Ali, N.M. El-Gohary, A.M. El-Kazak, Eur. J. Chem. 4 (2013) 311–328.
[15] M.A. Ibrahim, H.M. Hassanin, M. Abbas, S. Badran, Ark. iv (2013) 424–431.
[16] M.A. Ibrahim, H.M. Hassanin, Y.A. Gabr, Y.A. Alnamer, Synth. Commun. 44 (2014) 3470–3482.
[17] H. El Harmoudi, L. El Gaini, E. Daoudi, M. Rhazi, Y. Boughaleb, M.A. El Mohammadi, A. Migalska-Zalas, M. Bakasse, Opt. Mater. 36 (2014) 1471–1477.
[18] H. Arslan, A. Demircan, E. Gokturk, Spectrochim. Acta A 69 (2008) 105–112.
[19] Y. El Kouari, A. Migalska-Zalas, A.K. Arof, B. Sahraoui, Opt. Quant. Electron. 47 (2015) 1091–1099.
[20] W. Dong, M. Yan, M. Zhang, Z. Liu, Y. Li, Anal. Chim. Acta 542 (2005) 186–192.
[21] C. Isarankura-Na-Ayudhya, C. Nantasenamat, P. Buraparuangsang, T. Piacham, L. Ye, L. Bulow, V. Prachayasittikul, Molecules 13 (2008) 3077–3091.
[22] Y. Dineiro, M.I. Menendez, M.C. Blanco-Lopez, M.J. Lobo-Castanon, A.J. Miranda-Ordieres, P. Tunon-Blanco, Anal. Chem. 77 (2005) 6741–6746.
[23] W. Dong, M. Yan, Z. Liu, G. Wu, Y. Li, Sep. Purif. Technol. 53 (2007) 183–188.
[24] W.L. Jorgensen, Science 303 (2004) 1813–1818.
[25] T. Zhou, D. Huang, A. Caflisch, Curr. Top. Med. Chem. 10 (2010) 33–45.
[26] J.T. Kim, A.D. Hamilton, C.M. Bailey, R.A. Domoal, L. Wang, K.S. Anderson, W.L. Jorgensen, J. Am. Chem. Soc. 128 (2006) 15372–15373.
[27] (a) A.D. Becke, J. Chem. Phys. 98 (1993) 5648–5652;
(b) A.D. Becke, J. Chem. Phys. 98 (1993) 1372–1377.
[28] (a) C. Lee, W. Yang, R.G. Parr, Phys. Rev. B 37 (1988) 785–789;
(b) B. Miehlich, A. Savin, H. Stolt, H. Preuss, Chem. Phys. Lett. 157 (1989) 200–206.
[29] B. B. Stefanov, G. Liu, A. Liashenko, P. Piskorz, I. Komaromi, R. L. Martin, D. J. Fox, T. Keith, M. A. Al-Laham, C. Y. Peng, A. Nanayakkara, M. Challacombe, P. M. W. Gill, B. Johnson, W. Chen, M. W. Wong, C. Gonzalez, J. A. Pople, Gaussian, Inc., Pittsburgh PA. 2003.
[30] M. J. Frisch, G. W. Trucks, H. B. Schlegel, G, E. Scuseria, et al., Gaussian, Inc., Wallingford CT, 2009.
[31] R. Dennington, T. Keith, J. Millam, Gauss View, Semichem Inc., Shawnee Mission KS, 2009, Version 5. .
[32] http://www.chemcraftprog.com.
[33] M.A. Ibrahim, A.A.M. Farag, N. Roushdy, N.M. El-Gohary, J. Mol. Str. 1105 (2016) 370–380.
[34] V. Ganesh, I.S. Yahia, S. AlFaify, Mohd. Shkir, J. Phys. Chem. Solids 100 (2017) 115–125.
[35] H.M. Zeyada, M.I. Youssif, N.A. El-Ghamaz, M.E.O. Aboderbala, Phys. B 506 (2017) 75–82.
[36] M.M. El-Nahass, H.M. Abd El-Khalek, A.M. Nawar, Opt. Commun. 285 (2012) 1872–1881.
[37] J. Tauc, J. Non Cryst. Solids 149 (1987) 97–98.
[38] H. Saleem, A. Habib, J. Alloys Compd. 679 (2016) 177–183.
[39] D.I. Çifçia, T. Tunçala, A. Palab, O. Uslu, J. Photoch. Photobio. A 322–323 (2016) 102–109.
[40] S.R. Alharbi, A.A.A. Darwish, S.E. Al Garni, H.I. ElSaeedy, K.F. Abd El-Rahman, Infrared Phys. Tech. 78 (2016) 77–83.
[41] H.M. Zeyada, M.I. Youssif, N.A. El-Ghamaz, M.E.O. Aboderbal, Phys. B 506 (2017) 75–82.
[42] A. Ashery, A.A.M. Farag, M.A. Shenashen, Synth. Met. 162 (2012) 1357–1363.
[43] D. Cahen, A. Kahn, E. Umbach, Mater. Today 8 (2005) 32–41.
[44] K. Pabitra, N. Nayak, Periasamy, Org. Electron. 10 (2009) 1396–1400.
[45] C.S.J. Costa, R.J.S. Taveira, C.F.R.A.C. Lima, A. Mendes, L.M.N.B.F. Santos, Opt. Mater. 58 (2016) 51–60.
[46] M.C. Muiva, J.M. Mwabora, T.S. Sathiaraj, J.G. King, J. Alloys Compd. 689 (2016) 432–438.
[47] S.H. Wemple, Phys. Rev. B 7 (1973) 3767–3777.
[48] H.M. Zeyada, M.M. Makhlouf, M.I.M. Ismail, A.A. Salama, Mater. Chem. Phys. 163 (2015) 45–53.
[49] H.S. Soliman, E.F.M. El-Zaidia, H.A.M. Ali, S.M. Atef, Mater. Sci. Semicond. Proc. 26 (2014) 726–730.
[50] M.M. Makhlouf, H.M. Zeyada, Synth. Met. 211 (2016) 1–13.
[51] J. Robert, A. Mark, W. Alexander, J. Appl. Opt. 24 (1985) 3680–3682.
[52] A. Ashery, G. Said, W.A. Arafa, A.E.H. Gaballah, A.A.M. Farag, Synth. Met. 214 (2016) 92–99.
[53] A.A.M. Farag, A. Ashery, M. Shenashen, Phys. B 407 (2012) 2404–2411.
[54] A. Ashery, A.A.M. Farag, M. Shenashen, Synth. Met. 162 (2012) 1357–1363.
[55] A.A.M. Farag, I.S. Yahia, S. Alfaify, A. Bilgicli, M. Kandaz, F. Yakuphanoglu, Superlattice. Microst. 60 (2013) 83–100.
[56] M.M. El-Nahass, E.F. El-Deeb, H.S. Metwally, H.E.A. El-Sayed, A.M. Hassanein, Solid State Sci. 12 (2012) 552–557.
[57] S. Sarkar, N.S. Das, K.K. Chattopadhyay, Solid State Sci. 33 (2014) 58–66.
[58] J.I. Pankove, Optical Processes in Semiconductors, Dover Publications Inc., New York, 1975.
[59] F. Yakuphanoglu, A. Cukurovali, I. Yilmaz, Opt. Mater. 27 (2005) 1363–1368.
[60] R. Anuroop, B. Pradeep, J. Alloys Compd. 702 (2017) 432–441.
[61] G.D. Sharma, V.S. Choudhary, S.K. Sharma, M.S. Roy, J. Phys. Chem. Solids 69 (2008) 2639–2651.
[62] Z. Khurelbaatar, Y. Kil, H. Yun, K. Shim, J.T. Nam, K. Kim, S. Lee, C. Choi, J. Alloys Compd. 614 (2014) 323–329.
[63] G.D. Sharma, P. Balaraju, S.K. Sharma, M.S. Roy, Synth. Met. 158 (2008) 620–629.
[64] Q. Zhang, H. Guo, Z. Feng, L. Lin, J. Zhou, Z. Lin, Electrochim. Acta 55 (2010) 4889–4894.
[65] H.H. Guo, Zh.H. Lin, Z.F. Feng, L.L. Lin, J.Zh. Zhou, J. Phys. Chem. C 113 (2009) 12546–12550.